Effects of Nanoparticle Size on Cellular Uptake and Liver MRI with Polyvinylpyrrolidone-Coated Iron Oxide Nanoparticles

Jing Huang,[†,‡] Lihong Bu,[†,⊥] Jin Xie,[§] Kai Chen,[†] Zhen Cheng,[†] Xingguo Li,[‡,*] and Xiaoyuan Chen[†,§,*]

[†]Department of Radiology and Bio-X Program, Stanford University, 1201 Welch Road, P087, Stanford, California 94305, United States, [‡]Beijing National Laboratory for Molecular Sciences (BNLMS), (The State Key Laboratory of Rare Earth Materials Chemistry and Applications), College of Chemistry and Molecular Engineering, Peking University, Beijing 100871, P.R. China, [§]Laboratory of Molecular Imaging and Nanomedicine (LOMIN), National Institute of Biomedical Imaging and Bioengineering (NIBIB), National Institutes of Health (NIH), Bethesda, Maryland 20892, United States, and [⊥]Department of Radiology, The Fourth Hospital of Harbin Medical University, Heilongjiang, 150001, P.R. China

ABSTRACT The effect of nanoparticle size (30−120 nm) on magnetic resonance imaging (MRI) of hepatic lesions *in vivo* has been systematically examined using polyvinylpyrrolidone (PVP)-coated iron oxide nanoparticles (PVP-IOs). Such biocompatible PVP-IOs with different sizes were synthesized by a simple one-pot pyrolysis method. These PVP-IOs exhibited good crystallinity and high T_2 relaxivities, and the relaxivity increased with the size of the magnetic nanoparticles. It was found that cellular uptake changed with both size and surface physiochemical properties, and that PVP-IO-37 with a core size of 37 nm and hydrodynamic particle size of 100 nm exhibited higher cellular uptake rate and greater distribution than other PVP-IOs and Feridex. We systematically investigated the effect of nanoparticle size on MRI of normal liver and hepatic lesions *in vivo*. The physical and chemical properties of the nanoparticles influenced their pharmacokinetic behavior, which ultimately determined their ability to accumulate in the liver. The contrast enhancement of PVP-IOs within the liver was highly dependent on the overall size of the nanoparticles, and the 100 nm PVP-IO-37 nanoparticles exhibited the greatest enhancement. These results will have implications in designing engineered nanoparticles that are optimized as MR contrast agents or for use in therapeutics.

KEYWORDS: magnetic nanoparticles · iron oxide · magnetic resonance imaging · size dependent

Iron oxide (IO, Fe_3O_4 or γ-Fe_2O_3) nanostructured materials have attracted much attention because of their intriguing properties and wide applications in various fields, such as data storage,[1] catalysis,[2] sensors,[3] contaminant treatment,[4] and biomedicine.[5−14] Especially for the field of nanobiotechnology, IO nanomaterials have emerged as promising tools with increasing applications in detection and separation,[5] magnetic resonance imaging (MRI),[9−14] drug delivery,[6] hyperthermia therapy,[7] and tissue repair.[8] Tremendous efforts have been made in fabricating stable colloidal IO solutions with superior magnetic properties, good dispersibility, and biocompatibility−all of which are crucial for biomedical and clinical applications. Recent investigations impressively show that the magnetic properties of IO-based nanoparticles largely depend on particle size, natural crystallinity, chemical composition, and surface coating.[15−18] Meanwhile, enormous progress has also been achieved in alternative formulations and further functionalization of IOs to improve their dispersibility and biocompatibility, including surface exchange, ligand conjugation, and micelle encapsulation.[19−24] For instance, IO nanoparticles functionalized with dextran,[9] albumin,[10] silicones,[11] liposomes,[12] dendrimers[13] and poly(ethylene glycol)[14] have widely served as T_2 contrast agents that show high efficacy in enhancing images and enabling detection of focal lesions in living subjects through noninvasive, real-time MRI.

Recently, intensive research has been devoted to understanding the interaction between nanoparticles and biological systems in order to optimize their diagnostic sensitivity and therapeutic efficacy.[25,26] Various *in vitro* studies have demonstrated that particle size, surface chemistry, and physical shape greatly impact how nanoparticles interact with plasma proteins, cellular uptake, toxicity, and molecular response.[27−35] However, *in vivo* systems are far more complex than *in vitro* model systems, as the interactions of nanoparticles with biological components, such as proteins and cells, could change the final fate, kinetics and clearance of the nanoparticles. Generally speaking, nanoparticles with overall sizes in the range

*Address correspondence to shawn.chen@nih.gov, xgli@pku.edu.cn.

Received for review July 14, 2010 and accepted October 27, 2010.

Published online November 2, 2010. 10.1021/nn101643u

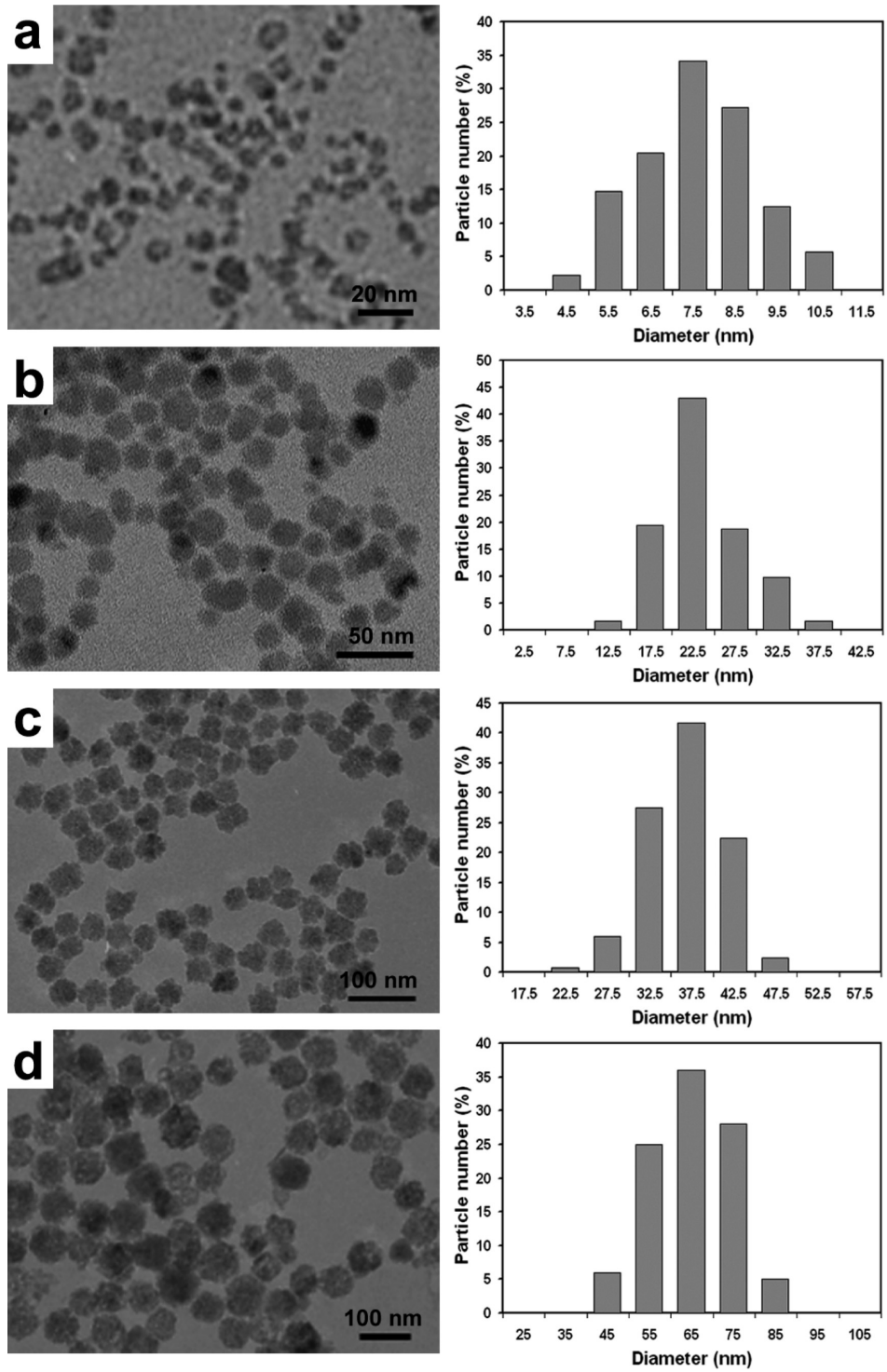

Figure 1. (Left) TEM images of as-synthesized IO nanoparticles: (a) PVP-IO-8, (b) PVP-IO-23, (c) PVP-IO-37, (d) PVP-IO-65. (Right) Corresponding particle size histograms obtained by statistical analysis of over ~150 particles.

of 10−200 nm are considered to be optimal for intravenous injection[19−21,23] The precise engineering parameters needed to build efficient MRI contrast agents have not been thoroughly identified, since few studies have systematically investigated the *in vivo* behavior of engineered nanostructures. Previous investigations have shown that the biodistribution is strongly dependent on the particle size, surface chemistry, and physical shape of the engineered nanostructures.[32,36] Kjems *et al*. examined the accumulation of PEGylated silane-coated IO nanoparticles in subcutaneous tumor, and found that larger nanoparticles tended to accumulate more effectively, resulting in stronger imaging contrast enhancement.[36] However, because of the lack of tests with a wide range of sizes, the specific influences of

particle size on *in vivo* biodistribution and MR imaging have not been fully investigated.

Herein, we systematically examined how particle design can be optimized toward efficient passive liver MR imaging. We synthesized a series of magnetite nanoparticles coated with polyvinylpyrrolidone (PVP) in different overall sizes, by tuning the reaction conditions we reported previously.[37] We then investigated how the size of nanoparticles affected their interactions with macrophage cells *in vitro*. Next, we examined size-dependent MR imaging of mouse liver *in vivo*, revealing a difference in behavior over the 30−120 nm size range. Finally, we examined enhancement of contrast in T_2-weighted MR imaging of an orthotopic liver tumor model. Through these systematic studies, we demonstrated that particle design has tremendous consequences on the distribution of nanoparticles in liver, which will allow for an optimized approach to liver MR imaging.

RESULTS AND DISCUSSION

PVP-coated iron oxide nanoparticles (PVP-IOs) were synthesized by the thermal decomposition of iron carbonyl ($Fe(CO)_5$) in *N*,*N*-dimethylformamide (DMF).[37] The particle size of the PVP-IOs was modulated by controlling the ratio of PVP to $Fe(CO)_5$. A decrease in particle size was observed by transmission electron microscopy (TEM) when the PVP concentration increased from 0.07 to 0.33 g/mL. Under other fixed reaction conditions, the highest PVP concentration (0.33 g/mL) resulted in particles with the smallest particle size, approximately 7.6 nm (Figure 1a). As the PVP concentration decreased to 0.27, 0.18, and 0.07 g/mL, the average particle size changed to 23.4 (Figure 1b), 36.8 (Figure 1c) and 65.3 nm (Figure 1d). For convenience, we labeled the samples as PVP-IO-8, PVP-IO-23, PVP-IO-37 and PVP-IO-65, respectively. PVP was immobilized on the surface of the IO nanocrystals *via* coordination interaction through its carbonyl group,[38] rendering the IO nanoparticles dispersible in water, as well as preventing them from having uncontrolled growth.

The hydrodynamic diameters of PVP-IO nanoparticles in aqueous solution were determined by dynamic light scattering (DLS) analysis (Figure 2). Compared to the particle sizes observed in TEM images, the corresponding hydrodynamic diameters of PVP-IO nanoparticles are much larger. The observed hydrodynamic diameter changed from 32.2 to 70.7, 102.4, and 118.3 nm as the core size of nanoparticles increased from 8 to 23, 37, and 65 nm, respectively. All the PVP-IOs are slightly positively charged while Feridex is negatively charged as indicated by the zeta potential measurement (see Table 1). These results are attributed to the hydrophilic polymer coating present on the surface, similar to the other reported formulations.[11,39,40] This biocompatible PVP coating may also enhance the blood circulation time and stabilize colloidal solution.[41]

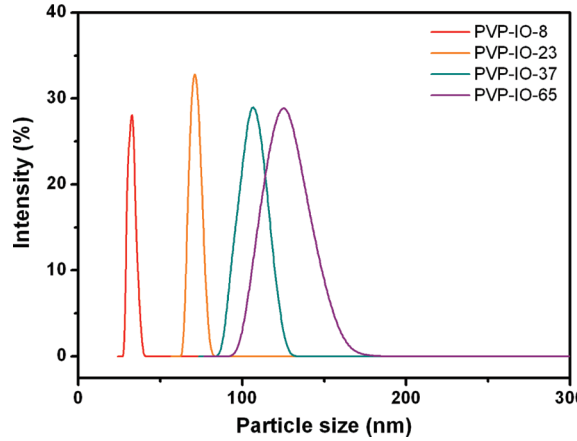

Figure 2. Hydrodynamic diameter distributions of PVP-IO samples determined by dynamic light scattering (DLS) measurements.

To evaluate the T_2 enhancing capabilities of the four PVP-IOs, aqueous solutions of the PVP-IOs at different Fe concentrations were investigated by T_2-weighted MRI on a 7.0 T small animal MR scanner (GE Healthcare). T_2-weighted phantom images decreased significantly in signal intensity with increasing Fe concentration, due to the dipolar interaction of the magnetic moments of the particles and protons in the water (Figure 3a), making the images darker. This behavior indicates that PVP-IOs generate MR contrast on T_2-weighted sequences, and are promising T_2 MRI contrast agents.

Figure 3b shows the relaxation rates, $1/T_2$, of PVP-IOs as a function of Fe concentration. The plots were well-fit by linear functions within the analyzed range of Fe concentration. It has been observed previously that relaxation rates vary linearly with Fe concentration:[42]

$$\frac{1}{T_2} = \frac{1}{T_2^0} + R_2[\mathrm{Fe}]$$

TABLE 1. Average Nanoparticle Size Determined by TEM, Average Hydrodynamic Diameter Obtained by DLS, Zeta Potential, and Corresponding R_2 Relaxation Values

samples	PVP:$Fe(CO)_5$	core size (nm)	HD size (nm)	zeta potential (mV)	R_2 (mM^{-1} s^{-1})
PVP-IO-8	1:6	7.6 ± 1.3	32.2 ± 2.2	12.7 ± 0.9	173.37
PVP-IO-23	1:7.5	23.4 ± 4.6	70.7 ± 3.5	11.9 ± 1.2	203.86
PVP-IO-37	1:12	36.8 ± 4.0	102.4 ± 6.2	13.7 ± 1.1	239.98
PVP-IO-65	1:15	65.3 ± 9.6	118.3 ± 12.0	12.5 ± 0.8	248.89
Feridex		4.8 ± 1.9	58.5 ± 185.8	−25.0 ± 1.3	127.48

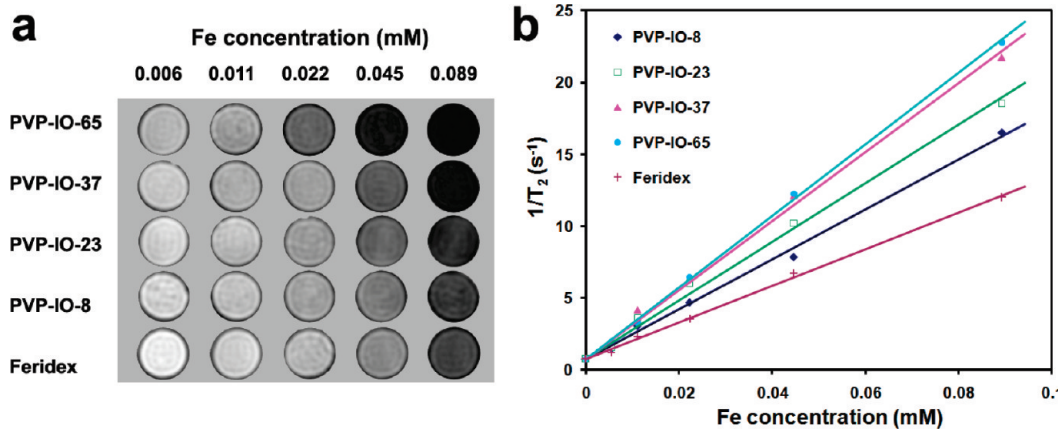

Figure 3. (a) T_2-weighted MR images of PVP-IOs in aqueous solution with various concentrations at 7 T; (b) graphs of $1/T_2$ against the Fe concentration for PVP-IOs, compared with Feridex.

where $1/T_2$ is the observed relaxation rate in the presence of magnetic nanoparticles, $1/T_2^0$ is the relaxation rate of pure water, and the product [Fe]R_2[39] is the relaxation by the field inhomogeneities, that is, the susceptibility effect induced by the magnetic ion ([Fe] is iron concentration and R_2 is the transverse relaxation rate, which represents the efficiency of the magnetic nanoparticles as a contrast agent). The specific relaxivity coefficients (R_2 values), determined by the slope of $1/T_2$ against Fe concentration, increase with increasing particle size, hence the R_2 value of PVP-IOs can be expressed as[43,44]

$$R_2 = \frac{1}{T_2^m} = \frac{a}{d_{NP}D}\gamma^2\mu^2 C_{NP}\, J(\omega, \tau_D)$$

where α is a constant, d_{NP} is the diameter of the nanoparticle, D is the diffusion coefficient, μ is the magnetic moment of the nanoparticles, γ is the gyromagnetic ratio of the water proton, C_{NP} is the concentration of the nanoparticles, and $J(\omega,\tau_D)$ is the spectral density function. According to the above equation, R_2 is proportional to the magnetic moment μ^2. Although magnetism is an intrinsic property of bulk materials, the magnetic properties of nanoparticles are strongly dependent on their size, shape, and surface properties.[18,45−47] Cheon and co-workers have systematically studied the relationships among size, magnetism, and relaxivity of uniform-sized IOs. It was found that larger IOs have a larger magnetization and higher R_2 relaxivity.[18,45,47] Thus, PVP-IO-65 nanoparticles, having the highest magnetic moments, will presumably distort the magnetic field most efficiently, and cause the greatest enhancement of the R_2 relaxation value. Indeed, as the PVP-IO size increased, R_2 steadily rose from approximately 173.37 to 203.86, 239.98, and 248.89 mM^{-1} s^{-1} for PVP-IO-8, PVP-IO-23, PVP-IO-37, and PVP-IO-65, respectively. Notably, the R_2 values for all PVP-IOs were found to be higher than that of the well-known commercial MRI contrast agent Feridex (127.48 mM^{-1} s^{-1}). The magnetic moment in IO is due to the localized electron density and hence strongly depends on the degree of crystallographic order.[48] As the synthetic procedure of PVP-IOs was performed at relatively high temperature compared to the alkaline coprecipitation method for Feridex, an improved crystallinity can be obtained.[37] This, in conjunction with the smaller core size and higher polydispersity of Feridex, explains the relatively higher relaxivities of PVP-IOs (see Table 1).

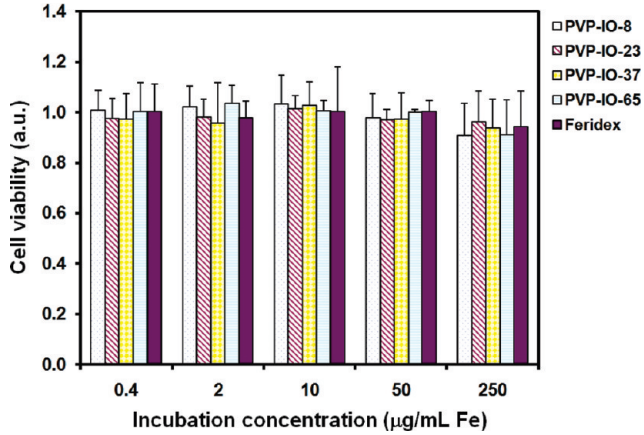

Figure 4. Cell viability of macrophage cells treated with various concentrations of PVP-IOs and Feridex measured by the MTT assay.

An MTT assay using mouse macrophage cell line RAW264.7 was performed to evaluate the cytotoxicity of PVP-IOs (Figure 4). PVP-IOs at six different concentrations, ranging from 0.4 to 250 μg Fe/mL, were incubated with macrophage cells for 24 h. The cell viability obtained by the MTT assay was expressed as a fraction of viable cells and normalized to that of cells without co-incubation with PVP-IOs (blank control). After incubation, the cell viability was maintained up to ~90% compared with the control. The MTT results indicate that the PVP-IOs showed little to no cytotoxicity even at the highest concentration (250 μg Fe/mL), which exceeds by 1 order of magnitude the concentrations of conventional iron-oxide-based-MRI contrast agents typically used in mice (1−20 mg/kg).[49]

To investigate the effect of size on cellular uptake, PVP-IOs solutions with various concentrations (0.4−250

μg Fe/mL) were co-incubated with macrophage cells for 1 h, and the quantitative amount of iron uptake was measured by ICP−AES. In Figure 5a, a plot of the amount of iron uptake by cells *versus* size of PVP-IOs showed that the cellular uptake was heavily dependent upon size, with the uptake of PVP-IO-37 > PVP-IO-65 > PVP-IO-8 > PVP-IO-23. The maximum uptake by cells occurred at a nanoparticle size of 37 nm, which was 1.3, 2.8, and 5.3 times the uptake of nanoparticles of size 65, 23, and 8 nm, respectively. Our result that 37 nm is the optimal size for cell uptake corresponds well to recent investigations of other particles. For instance, Chithrani *et al*. found that 50 nm gold nanoparticles with surfaces modified by citric acid had higher cellular uptake rates than 14 and 74 nm nanoparticles.[34] Lu *et al*. also found that, for a range of 30−280 nm mesoporous silica nanoparticles, 50 nm particles had the maximum uptake by HeLa cells.[35]

Figure 5b indicates that, in all the samples, the uptake of nanoparticles significantly increased in the first 4 h, but the uptake rate gradually slowed and reached a plateau at 4−8 h, depending on the size. This plateau effect is in agreement with a previous study by Chithrani *et al*.[34] The average uptake rates during the first 4 h were 1.17, 1.36, 2.06, 1.56, 0.76 pg/cell per hour for PVP-IO-8, PVP-IO-23, PVP-IO-37, PVP-IO-65, and Feridex, respectively. Compared with other IOs, PVP-IO-37 exhibits the highest uptake rate. It has been well-documented that the cellular uptake of substances can be affected by a group of factors, such as size, shape, surface charge, roughness, and functional groups on the surface.[27−35] Size, in particular, was found to be a critical criterion, and can in large part decide the exact mechanisms by which nanomaterials get internalized. It is generally acknowledged that substances in the range of 10−30 nm can diffuse across a plasma membrane freely or through membrane channels, while the larger particles are mainly carried into a cell by pinocytosis or phagocytosis.[30,50] Even within the latter category, the internalization pathway can still be different. As pointed out by Conner and Schmid, there are at least three types of endocytosis for nanoparticles: clathrin-mediated endocytosis, caveolae-mediated endocytosis, and clathrin- and caveolae-independent endocytosis.[50] The detailed mechanism for the uptake of PVP-IOs is not clear at this stage. However, it is clear that the uptake is size-dependent, and among all the four tested formulas, PVP-IO-37 demonstrated the fastest and highest uptake. On the contrary, Feridex showed a much slower uptake rate, which we attributed to its high polydispersity and its slightly negatively charged coating (in comparison to the slightly positively charged PVP coating).

Iron oxide nanoparticles have been extensively developed for liver MR imaging. The working mechanism is that the IOs, after i.v. administration, are rapidly taken up by the hepatic Kupffer cells, resulting in a decrease of MR signal intensity by shortening proton T_2 relaxation times in the neighborhood. To first assess the *in vivo* MRI effects of PVP-IOs, we performed T_2-weighted MRI in normal, healthy Balb/c mice before and after administration of PVP-IOs. The intravenous dose was 2.5 mg Fe (measured by ICP-AES) per kg of mouse body weight, and a 7.0 T MRI apparatus was used to collect data from the liver. To quantify the contrast enhancement, regions of interest (ROIs) (Supporting Information, Figure S1) were selected on the T_2-weighted MR images of the liver (Figure 6). The signal-to-noise ratio (SNR) was calculated according to the equation: liver signal-to-noise ratio $SNR_{liver} = SI_{liver}/SD_{noise}$, (where SI stands for signal intensity and SD stands for standard deviation) and the average relative liver signal intensities of mice (SNR_{post}/SNR_{pre}) were plotted at different time points (Figure 7a). Relative contrast enhancement was defined as signal decrease $\Delta SNR = (SNR_{pre} - SNR_{post})/SNR_{pre}$. Compared with the preimages, the images taken 10 min after administration showed some hypointensities in the liver, which maximized at 1 h time point. ΔSNR values of the PVP-IO-37, PVP-IO-65, and Feridex were significantly larger than those of PVP-IO-8 and PVP-IO-23. It has been previously reported that the relaxivity of magnetic nanoparticles is size-dependent, which grows as particle size increases.[18,45,47]

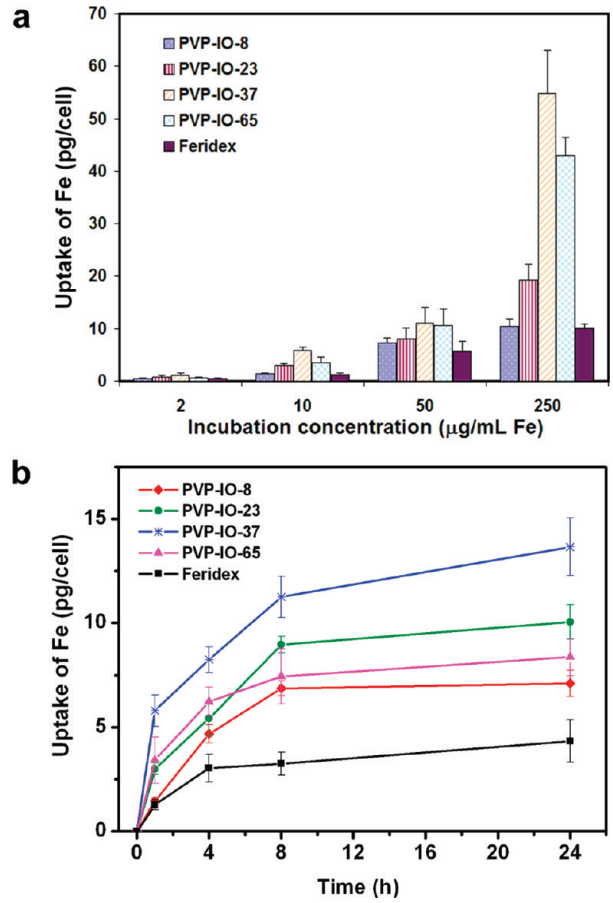

Figure 5. (a) Cellular uptake of PVP-IOs and Feridex by macrophage cells at various concentrations with an incubation time of 1 h. (b) Cellular uptake of PVP-IOs and Feridex by macrophage cells as a function of incubation time at Fe concentration of 10 μg/mL.

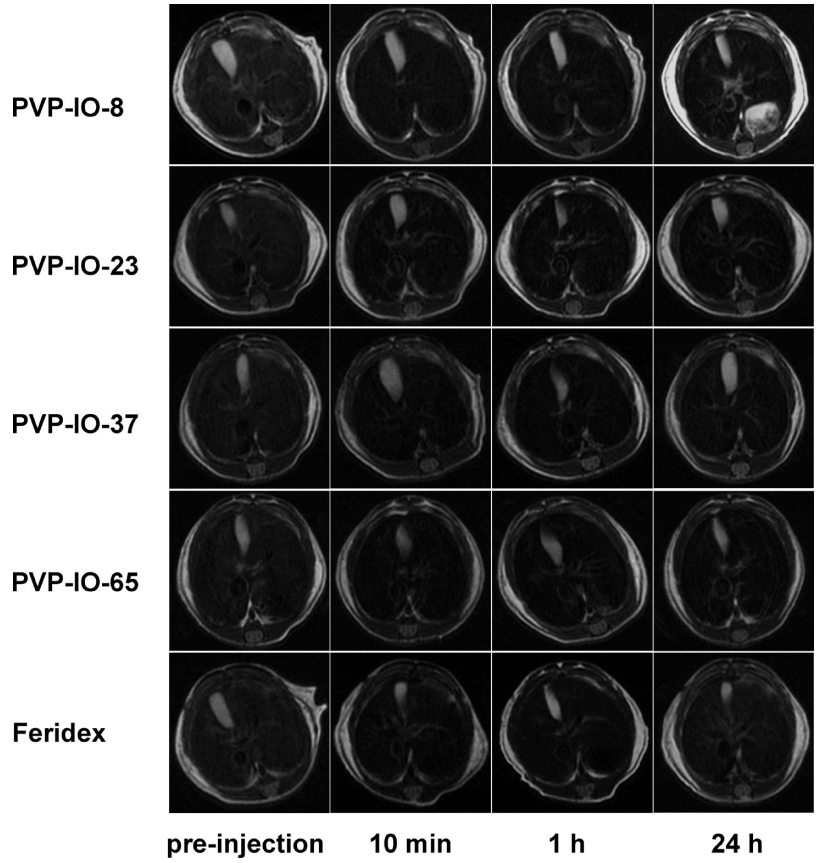

Figure 6. *In vivo* mouse liver MR images at different time points after intravenous administration of PVP-IOs and Feridex at a dose of 2.5 mg/kg.

On the other hand, the cellular uptake of nanoparticles, also being size-dependent, maximizes at a certain value, as reported by other groups[34,35] and observed in the current study. Both factors are believed to play a role in determining the liver contrast enhancement. The relatively lower contrast enhancement of smaller nanoparticles (PVP-IO-8 and PVP-IO-23) is likely attributed to their rapid depletion from the bloodstream, their lower uptake into Kupffer cells, and their naturally smaller relaxivities, while the outperformance of PVP-IO-37 is due to the close-to-maximum R_2 and the best macrophage engulfment. The Prussian blue staining results confirmed that the "darkening" in the liver was caused by IO nanoparticle accumulation (Supporting Information, Figure S2).

We then looked at the *in vivo* effects of Feridex on MRI. Prior research has shown that clearance by the RES cells in the liver and spleen of rats becomes saturated when more than 10^{15} particles are injected in a single bolus.[51] To avoid saturation, we injected at a dose of 1.0 or 2.5 mg Fe/kg, a dose which is at least 100 times less concentrated (with the assumption that the organ weight of mice is approximately one-tenth that of rats). At 1 h after administration, the ΔSNR of PVP-IO-37 was slightly higher than those of PVP-IO-65 and Feridex at both doses (Figure 7a,b). However, the advantage is not as dramatic compared with their difference in uptake at the *in vitro* level. Such a result was attributable to the complicated *in vivo* environment. During circulation, the particles may tangle with serum proteins or form aggregates, both of which will lead to an increased overall particle size which causes them to defy the predicated behavior. Nonetheless, the significant signal intensity (SI) changes induced by PVP-IO-37 promise its use in identifying small focal hepatic lesions, including tumor metastases.

To evaluate the efficacy of the PVP-IOs in enhancing MRI contrast in hepatic lesions, *in vivo* MR images were evaluated with nude mice bearing orthotopic Huh7 liver cancer before and after administration of PVP-IO-37 and Feridex, with a dose of 1.0 mg Fe/kg of body weight (Figure 8). Since hepatic tumors either do not contain RES cells or the activity of their RES cells is reduced, they do not accumulate nanoparticles as efficiently as normal tissue.[52,53] Thus the tumor cells appear as bright spots on a T_2- or T_2*-weighted image, against surrounding normal tissues which undergo particle accumulation and are manifested as hypo-intensities. Regions of interest were selected around the tumor and liver parenchyma for measurement of the signal intensity. Contrast-to-noise ratio (CNR) was defined as $CNR = (SNR_{tumor} - SNR_{liver})/SNR_{tumor}$ with $SNR = SI_{mean}/SD_{noise}$, where SI denotes the tumor or liver intensity and SD is the standard deviation of the noise in the image. The in-

crease in tumor-to-liver contrast is defined as $\Delta CNR = (CNR_{post} - CNR_{pre})/CNR_{pre}$. We observed, at the 1 h time point, a contrast change (ΔCNR) of 81 ± 8% with the commercial Feridex, which was lower than that of the PVP-IO-37 (94 ± 6%) (Figure 9). This was consistent with the observation from normal mice. As discussed above, compared with the surrounding normal liver tissue, a tumor tends to have a low IO nanoparticle uptake. Such a difference caused a less dramatic signal drop in the tumor area and was manifested as a contrast between tumor and normal tissue on T_2/T_2*-weighted MR images.

CONCLUSIONS

Water-soluble IO nanoparticles ranging from 8−65 nm in diameter were synthesized in strongly polar solvent DMF by controlling the surfactant PVP concentration. These PVP-IOs exhibit higher T_2 relaxivities compared to Feridex, due to their higher crystallinity. The relaxivity R_2 increases with the size of the magnetic nanoparticles. We also examined the influence of particle size on the uptake of PVP-IOs by macrophage cells. It was found that the cellular uptake is dependent on particle size, and the maximum uptake by cells occurs at a nanoparticle size of 37 nm (PVP-IO-37). We systematically examined the effect of particle size on MRI of normal liver and hepatic lesions *in vivo*, and found that the MRI contrast enhancement of PVP-IOs within liver is highly dependent on the size of the particles. MRI studies *in vivo* indicated that PVP-IO-37 nanoparticles with an overall size of 100 nm exhibited the highest contrast enhancement. T_2-weighted signal intensity in mouse liver decreased about 67% at 1 h (thereby increasing the contrast with hepatic lesions by about 94%) after intravenous administration of PVP-IO-37. Our results provide optimized design parameters for engineering nanoparticles to be applied in biomedical imaging and therapeutics. Detailed investigations of the effects of nanoparticle size on the diagnosis of other diseases of the liver by MRI are currently in progress.

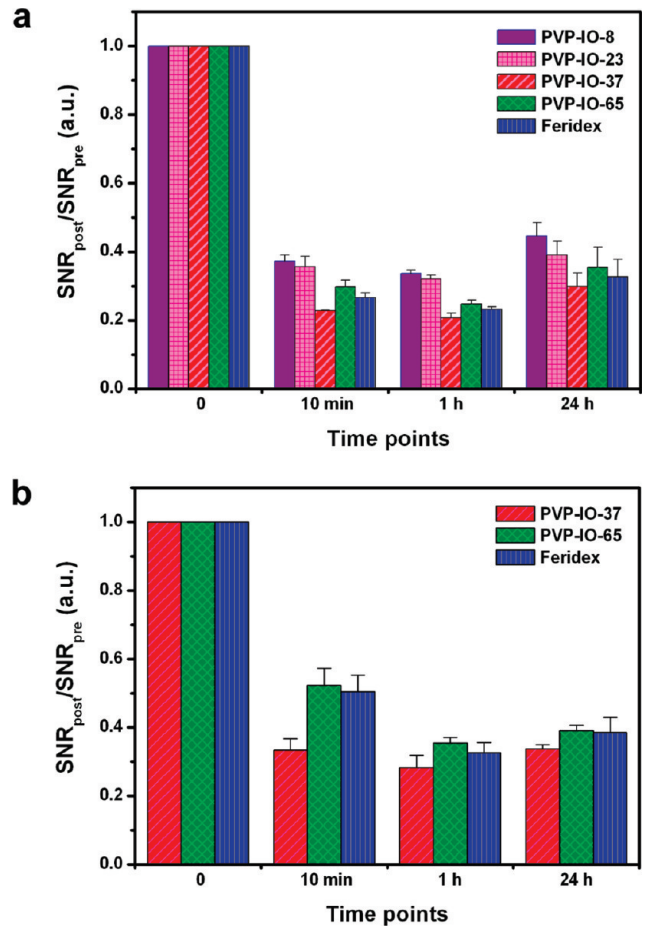

Figure 7. Quantification of relative SNR_{liver} collected before and after administration of PVP-IOs in normal, healthy Balb/c mice (n = 3/group), compared with Feridex, at the dose of (a) 2.5 mg Fe/kg and (b) 1.0 mg Fe/kg.

METHODS

Preparation of PVP-Coated Iron Oxide Nanoparticles (PVP-IOs). PVP-IOs were synthesized according to our previously described method[37] with some modifications. Uniform-sized PVP-IO nanoparticles were synthesized by thermal decomposition of iron carbonyl ($Fe(CO)_5$, 99.999%, Aldrich). Typically, 5 g of polyvinylpyrrolidone (PVP, MW = 10000, Sigma-Aldrich) was dissolved in 15 mL of anhydrous dimethylformamide (DMF, 99.8%, Sigma-Aldrich). The resulting solution was then purged with argon for 30 min at room temperature to remove oxygen and subsequently heated to 160 °C under an inert argon atmosphere. As the temperature reached 160 °C, 0.4 mL of $Fe(CO)_5$ (~3 mmol) was quickly injected into the mixture under vigorous stirring. The reaction mixture was maintained at 160 °C for 2 h. The initially transparent red-brown solution became light brown and gradually turned black-brown. The final black-brown colloid solution was then stirred for another 1 h, cooled to room temperature, and destabilized by adding 50 mL of acetone. The precipitate was collected by centrifugation and washed twice to remove excess surfactant and reaction byproducts. The particles were then resuspended in water and dialyzed with deionized water for 24 h. The size of the PVP-IO nanoparticles could be controlled by varying the ratio of PVP to $Fe(CO)_5$. PVP-IOs with particle sizes of 8, 23, 37, and 65 nm were obtained when the ratio of PVP to $Fe(CO)_5$ was 1:6, 1:7.5, 1:12, and 1:15, respectively.

Characterization of PVP-IOs. Particle size and morphology were examined by using a JEOL JEM-2010 analytical transmission electron microscope. PVP-IOs solutions were diluted with deionized water, added dropwise onto a carbon-coated copper grid, and dried for TEM analysis. The hydrodynamic sizes of the PVP-IOs were investigated using the diluted solutions on an electrophoretic light scattering spectrophotometer (Otsuka electronics, Photal ELS-8000). The zeta potentials were measured on Zetasizer Nano ZS (Malvern Instruments Ltd., Worcestershire, UK) at room temperature in water. The concentrations of PVP-IO solutions were determined by inductively coupled plasma atomic emission spectroscopy (ICP−AES) (TJA IRIS Advantage/1000 Radial ICAP spectrometer). For that purpose, the PVP-IOs were predecomposed with nitric acid (HNO_3) to be converted to Fe(III) solution.

Measuring MRI Relaxation Properties of PVP-IOs. To confirm the feasibility of the size-tuned water dispersed PVP-IOs as MRI contrast agents, we first prepared a ferrofluid phantom. We prepared 200 μL tubes of PVP-IOs and Feridex (40 μmol Fe/kg, Berlex Laboratories) with Fe concentrations varying from 0.006 to 0.089 mM. These tubes containing samples were embedded in a phantom which consisted of tanks filled with 1% agarose gel

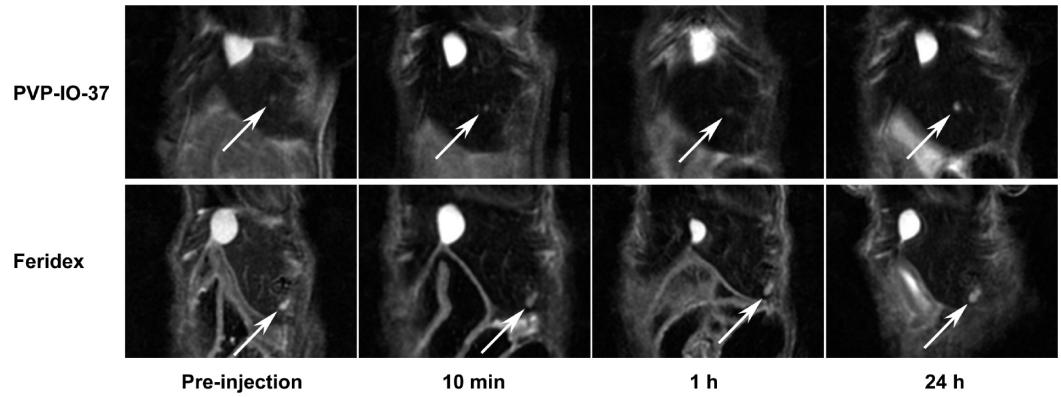

Figure 8. MR images of Huh7 orthotropic liver cancer model at different time points after intravenous administration of PVP-IO-37 and Feridex (1 mg Fe/kg). Arrows indicate the pseudopositive contrast from the tumor.

to obtain appropriate images. MRI was performed using a 7.0 T small animal MRI scanner (GE Healthcare) equipped with a homemade surface coil. The MR image was obtained by a T_2 spin echo sequence (repetition time (TR) = 3000 ms, echo time (TE) = 10, 20, 40, 60, 80, 100, 120 ms, matrix = 128 × 128, field of view (FOV) = 5.0 × 5.0 cm^2, slice thickness =1.00 mm, number of excitation (NEX) = 1). The signal intensities of each ROI (region-of-interest) in the T_2 map were measured for each concentration; these were then used for R_2 calculations using an RT-imaging program.

***In Vitro* Cytotoxicity Evaluation.** Mouse macrophage cell line RAW264.7 was obtained from American type culture collection (ATCC, Manassas, VA) and cultured following the manufacturer's instructions. *In vitro* cytotoxicity of the IOs was assessed by the 3-(4,5-dimethylthiazol-2-yl)-2,5-iphenyltetrazolium bromide (MTT) assay. For *in vitro* cytotoxic assay, cells were detached and plated in 96-well flat-bottom microplates at 1000−10000 cells per well. After 24 h recovery at 37 °C, the medium was replaced with 200 μL medium containing IOs of various concentrations (the equivalent Fe concentrations were 250, 50, 10, 2, and 0.4 μg Fe/mL). For control, the same volume of pure culture medium was included in each experiment. After 24 h incubation at 37 °C, the nanoparticle suspension was removed and the cells were washed twice with PBS. After that, 90 μL medium and 10 μL MTT solution were added to each well, and the cells were incubated for another 3 h. After the incubation, the supernatant was removed and 100 μL dimethylsulfoxide (DMSO) was added to each well to dissolve the formazan crystals. Finally, a microplate reader was used to measure the absorbance of all the samples (n = 5 per group). Cell viabilities were determined by comparing the absorbance of the cells incubated with the IOs to the absorbance of cells serving as controls.

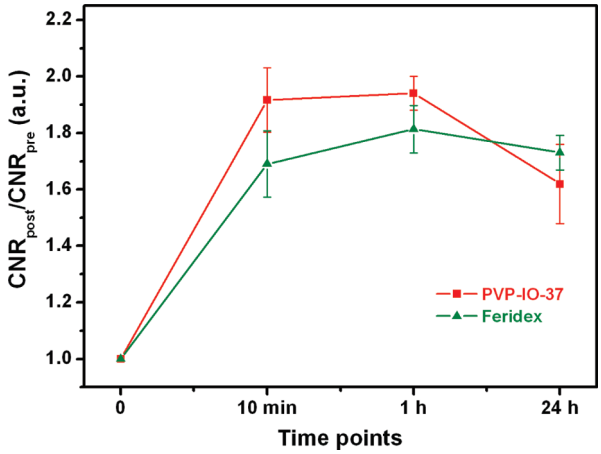

Figure 9. Mean values of relative CNR in MR images on orthotropic liver cancer model before and after administration of PVP-IO-37 nanoparticles, compared with Feridex, at the dose of 1.0 mg Fe/kg (n = 3/group).

Cellular Uptake. The RAW264.7 mouse macrophage cells were seeded at 5 × 10^5 cells/well in a 6-well plate. After 24 h attachment, the cells were treated with medium containing IOs of various concentrations for different incubation times at 37 °C. Then, the cells were washed with phosphate-buffered saline (PBS) three times and trypsinized. After centrifugation, the cell pellet was washed once. The cells were resuspended in medium and were counted carefully. Then, concentrated nitric acid (HNO_3) was added to dissolve the cells at 70 °C. These clear acidic solutions (n = 3 per group) were diluted to determine the concentration of Fe by ICP−AES.

Animal Preparation and *In Vivo* MRI Testing. Human hepatoma cell line Huh7 was purchased from the American Type Culture Collection (ATCC, Manassas, VA) and cultured with ATCC-formulated Eagle's Minimum Essential Medium in a cell culture incubator. Balb/c mice and athymic nude mice were purchased from Harlan Laboratories (Indianapolis, IN). Approximately 5 × 10^6 Huh7 cells were inoculated subcutaneously into the front flank of each nude mouse, and the tumor was harvested 3 weeks after tumor inoculation. Orthotopic liver HCC tumors were established by inoculation of small subcutaneous tumor fragments into the left liver lobe of nude mice during laparotomy with anesthesia by 2% isoflurane in oxygen-enriched air. Single tumor nodules (~1 mm in diameter) were observed in the liver under the MRI scanning (about 7 days after inoculation). All the animal work was conducted following a protocol approved by Stanford University Administrative Panel on Laboratory Animal Care (APLAC).

To observe the *in vivo* MRI effect, T_2-weighted MRI was performed in normal, healthy Balb/c mice weighing 20−30 g. The mice were anesthetized by breathing 2% isoflurane in oxygen-enriched air with a facemask. The PVP-IOs and Feridex were administered into the tail vein of each mouse with a dose of 2.5 mg (1.0 mg of Fe, as measured by ICP−AES) per kg of mouse body weight. For the orthotopic xenograft tumor model, the selected PVP-IOs and Feridex were administered through the tail vein of each mouse with a dose of 1.0 mg of Fe (measured by ICP-AES) per kg of mouse body weight. The T_2-weighted MR images of the liver were obtained with a TSE technique using a 7.0 T small animal MRI scanner (GE Healthcare) equipped with a homemade surface coil. The sequence parameters were (repetition time (TR) = 3000 ms, echo time (TE) = 40 ms, matrix= 256 × 256, field of view (FOV) = 6.0 × 6.0 cm^2, slice thickness =1.00 mm, number of excitation (NEX) = 6). The MRI signals were serially obtained at preinjection, and at 10 min, 1 h, and 24 h after administration of PVP-IOs or Feridex. To evaluate the contrast, signal intensities (SI) of normal liver parenchyma, hepatic lesions, and background noises were measured before and after injection of IOs. The mean SI measurements of 3 mice per group were used for statistical analysis. SI were obtained in defined regions of interest (ROIs) by imaging analysis software Oxsis (National Institutes of Health). Because of slight changes in the position of the mice at different imaging stages, pre and post ROIs were defined manually on each image as reproducibly as possible. For

each animal, 3 ROIs were selected to measure the SI of the liver, devoid of large vessels, prominent artifact, or focal changes in SI. For hepatic lesions, a circular ROI was drawn to encompass as much of the lesion as possible. The standard deviation (SD) of background noise was measured in the largest possible ROI positioned in the phase-encoding direction outside the abdominal wall in order to account for any motion artifacts. To plot the time course of the signal enhancement, the signal-to-noise ratio (SNR) and the lesion-to-liver contrast-to-noise ratio (CNR) were calculated according to the equation: signal-to-noise ratio $SNR = SI_{mean}/SD_{noise}$; and lesion-to-liver $CNR = (SNR_{lesion} - SNR_{liver})/SNR_{tumor}$. Relative contrast enhancement at different time points was defined as signal decrease $\Delta SNR = (SNR_{pre} - SNR_{post})/SNR_{pre}$. The increase in tumor-to-liver contrast was defined as $\Delta CNR = (CNR_{post} - CNR_{pre})/CNR_{pre}$.

Prussian Blue Staining. Six animals were separately injected with the PVP-IOs and Feridex and then sacrificed for extracting tissues from liver parenchyma. The harvested tissues were placed into OCT using a plastic mold and the samples were immediately frozen using dry ice and placed into liquid nitrogen. Tissue sections were cut into 10 μm-thick slices. Standard fixing and Prussian blue staining protocols were then used. The principle of this method is that ferric iron (Fe^{3+}) in the presence of ferrocyanide ion is precipitated as the highly colored and highly water-insoluble complex, potassium ferric ferrocyanide, Prussian blue. Briefly, the tissue slices were fixed with acetone, incubated with 10% potassium ferrocyanide in 20% hydrochloric acid, and subsequently washed with PBS buffer three times. For counterstaining with nuclear fast red, the slices were incubated with 1% eosin solution and washed with PBS buffer. The slices were dehydrated by incubation with absolute ethanol and xylene. The iron particles in the slices were observed as blue dots using an optical microscope with phase contrast.

Acknowledgment. This research was supported in part by the Intramural Research Program of the NIH, including the National Institute of Biomedical Imaging and Bioengineering, by the National Science Foundation of China (NSFC) (No. 20971009 and 20821091), and by the Ministry of Science and Technology (MOST) of China (No. 2009CB939902 and 2010CB631301). We thank Dr. Henry S. Eden for proof-reading the manuscript.

Supporting Information Available: Examples of regions of interest (ROIs) selected on an *in vivo* MR image at mouse liver site; Prussian blue staining of liver and spleen harvested at 1 h after administration of different PVP-IOs and Feridex at the dose of 2.5 mg/kg per mouse weight. This material is available free of charge *via* the Internet at http://pubs.acs.org.

REFERENCES AND NOTES

1. Frey, N. A.; Peng, S.; Cheng, K.; Sun, S. H. Magnetic Nanoparticles: Synthesis, Functionalization, and Applications in Bioimaging and Magnetic Energy Storage. *Chem. Soc. Rev.* **2009**, *38*, 2532–2542.
2. Zhang, D. H.; Li, G. D.; Li, J. X.; Chen, J. S. One-Pot Synthesis of Ag-Fe_3O_4 Nanocomposite: A Magnetically Recyclable and Efficient Catalyst for Epoxidation of Styrene. *Chem. Commun. (Cambridge, U.K.)* **2008**, 3414–3416.
3. Sljukic, B.; Banks, C. E.; Compton, R. G. Iron Oxide Particles Are the Active Sites for Hydrogen Peroxide Sensing at Multiwalled Carbon Nanotube Modified Electrodes. *Nano Lett.* **2006**, *6*, 1556–1558.
4. Shin, S.; Jang, J. Thiol Containing Polymer Encapsulated Magnetic Nanoparticles as Reusable and Efficiently Separable Adsorbent for Heavy Metal Ions. *Chem. Commun. (Cambridge, U.K.)* **2007**, 4230–4232.
5. Gu, H. W.; Xu, K. M.; Xu, C. J.; Xu, B. Biofunctional Magnetic Nanoparticles for Protein Separation and Pathogen Detection. *Chem. Commun. (Cambridge, U.K.)* **2006**, 941–949.
6. Piao, Y.; Kim, J.; Bin Na, H.; Kim, D.; Baek, J. S.; Ko, M. K.; Lee, J. H.; Shokouhimehr, M.; Hyeon, T. Wrap−Bake−Peel Process for Nanostructural Transformation from β-FeOOH Nanorods to Biocompatible Iron Oxide Nanocapsules. *Nat. Mater.* **2008**, *7*, 242–247.
7. Sonvico, F.; Mornet, S.; Vasseur, S.; Dubernet, C.; Jaillard, D.; Degrouard, J.; Hoebeke, J.; Duguet, E.; Colombo, P.; Couvreur, P. Folate-Conjugated Iron Oxide Nanoparticles for Solid Tumor Targeting as Potential Specific Magnetic Hyperthermia Mediators: Synthesis, Physicochemical Characterization, and *in Vitro* Experiments. *Bioconjugate Chem.* **2005**, *16*, 1181–1188.
8. Heymer, A.; Haddad, D.; Weber, M.; Gbureck, U.; Jakob, P. M.; Eulert, J.; Noth, U. Iron Oxide Labelling of Human Mesenchymal Stem Cells in Collagen Hydrogels for Articular Cartilage Repair. *Biomaterials* **2008**, *29*, 1473–1483.
9. Moore, A.; Marecos, E.; Bogdanov, A.; Weissleder, R. Tumoral Distribution of Long-Circulating Dextran-Coated Iron Oxide Nanoparticles in a Rodent Model. *Radiology* **2000**, *214*, 568–574.
10. Xie, J.; Wang, J. H.; Niu, G.; Huang, J.; Chen, K.; Li, X. G.; Chen, X. Y. Human Serum Albumin Coated Iron Oxide Nanoparticles for Efficient Cell Labeling. *Chem. Commun. (Cambridge, U.K.)* **2010**, *46*, 433–435.
11. Tan, H.; Xue, J. M.; Shuter, B.; Li, X.; Wang, J. Synthesis of PEOlated Fe_3O_4@SiO_2 Nanoparticles *via* Bioinspired Silification for Magnetic Resonance Imaging. *Adv. Funct. Mater.* **2010**, *20*, 722–731.
12. Bruns, O. T.; Ittrich, H.; Peldschus, K.; Kaul, M. G.; Tromsdorf, U. I.; Lauterwasser, J.; Nikolic, M. S.; Mollwitz, B.; Merkell, M.; Bigall, N. C. Real-Time Magnetic Resonance Imaging and Quantification of Lipoprotein Metabolism *in Vivo* Using Nanocrystals. *Nat. Nanotechnol.* **2009**, *4*, 193–201.
13. Shi, X. Y.; Wang, S. H.; Swanson, S. D.; Ge, S.; Cao, Z. Y.; Van Antwerp, M. E.; Landmark, K. J.; Baker, J. R. Dendrimer-Functionalized Shell-Crosslinked Iron Oxide Nanoparticles for *in Vivo* Magnetic Resonance Imaging of Tumors. *Adv. Mater.* **2008**, *20*, 1671–1678.
14. Tromsdorf, U. I.; Bruns, O. T.; Salmen, S. C.; Beisiegel, U.; Weller, H. A Highly Effective, Nontoxic T-1 MR Contrast Agent Based on Ultrasmall PEGylated Iron Oxide Nanoparticles. *Nano Lett.* **2009**, *9*, 4434–4440.
15. Duan, H. W.; Kuang, M.; Wang, X. X.; Wang, Y. A.; Mao, H.; Nie, S. M. Reexamining the Effects of Particle Size and Surface Chemistry on the Magnetic Properties of Iron Oxide Nanocrystals: New Insights into Spin Disorder and Proton Relaxivity. *J. Phys. Chem. C* **2008**, *112*, 8127–8131.
16. Tromsdorf, U. I.; Bigall, N. C.; Kaul, M. G.; Bruns, O. T.; Nikolic, M. S.; Mollwitz, B.; Sperling, R. A.; Reimer, R.; Hohenberg, H.; Parak, W. J. Size and Surface Effects on the MRI Relaxivity of Manganese Ferrite Nanoparticle Contrast Agents. *Nano Lett.* **2007**, *7*, 2422–2427.
17. Casula, M. F.; Floris, P.; Innocenti, C.; Lascialfari, A.; Marinone, M.; Corti, M.; Sperling, R. A.; Parak, W. J.; Sangregorio, C. Magnetic Resonance Imaging Contrast Agents Based on Iron Oxide Superparamagnetic Ferrofluids. *Chem. Mater.* **2010**, *22*, 1739–1748.
18. Jun, Y. W.; Seo, J. W.; Cheon, A. Nanoscaling Laws of Magnetic Nanoparticles and Their Applicabilities in Biomedical Sciences. *Acc. Chem. Res.* **2008**, *41*, 179–189.
19. Corot, C.; Robert, P.; Idee, J. M.; Port, M. Recent Advances in Iron Oxide Nanocrystal Technology for Medical Imaging. *Adv. Drug Delivery Rev.* **2006**, *58*, 1471–1504.
20. Gupta, A. K.; Gupta, M. Synthesis and Surface Engineering of Iron Oxide Nanoparticles for Biomedical Applications. *Biomaterials* **2005**, *26*, 3995–4021.
21. Xie, J.; Huang, J.; Li, X.; Sun, S.; Chen, X. Iron Oxide Nanoparticle Platform for Biomedical Applications. *Curr. Med. Chem.* **2009**, *16*, 1278–1294.
22. Latham, A H.; Williams, M. E. Controlling Transport and Chemical Functionality of Magnetic Nanoparticles. *Acc. Chem. Res.* **2008**, *41*, 411–420.
23. Laurent, S.; Forge, D.; Port, M.; Roch, A.; Robic, C.; Elst, L. V.; Muller, R. N. Magnetic Iron Oxide Nanoparticles: Synthesis, Stabilization, Vectorization, Physicochemical Characterizations, and Biological Applications. *Chem. Rev.* **2008**, *108*, 2064–2110.

24. Amstad, E.; Zurcher, S.; Mashaghi, A.; Wong, J. Y.; Textor, M.; Reimhult, E. Surface Functionalization of Single Superparamagnetic Iron Oxide Nanoparticles for Targeted Magnetic Resonance Imaging. *Small* **2009**, *5*, 1334–1342.
25. Nel, A. E.; Madler, L.; Velegol, D.; Xia, T.; Hoek, E. M. V.; Somasundaran, P.; Klaessig, F.; Castranova, V.; Thompson, M. Understanding Biophysicochemical Interactions at the Nano−Bio Interface. *Nat. Mater.* **2009**, *8*, 543–557.
26. Perrault, S. D.; Walkey, C.; Jennings, T.; Fischer, H. C.; Chan, W. C. W. Mediating Tumor Targeting Efficiency of Nanoparticles through Design. *Nano Lett.* **2009**, *9*, 1909–1915.
27. Aggarwal, P.; Hall, J. B.; McLeland, C. B.; Dobrovolskaia, M. A.; McNeil, S. E. Nanoparticle Interaction with Plasma Proteins as It Relates to Particle Biodistribution, Biocompatibility, and Therapeutic Efficacy. *Adv. Drug Delivery Rev.* **2009**, *61*, 428–437.
28. Luciani, N.; Gazeau, F.; Wilhelm, C. Reactivity of the Monocyte/Macrophage System to Superparamagnetic Anionic Nanoparticles. *J. Mater. Chem.* **2009**, *19*, 6373–6380.
29. Thorek, D. L. J.; Tsourkas, A. Size, Charge and Concentration Dependent Uptake of Iron Oxide Particles by Non-phagocytic Cells. *Biomaterials* **2008**, *29*, 3583–3590.
30. Verma, A.; Stellacci, F. Effect of Surface Properties on Nanoparticle−Cell Interactions. *Small* **2010**, *6*, 12–21.
31. Jiang, W.; Kim, B. Y. S.; Rutka, J. T.; Chan, W. C. W. Nanoparticle-Mediated Cellular Response is Size-Dependent. *Nat. Nanotechnol.* **2008**, *3*, 145–150.
32. He, C. B.; Hu, Y. P.; Yin, L. C.; Tang, C.; Yin, C. H. Effects of Particle Size and Surface Charge on Cellular Uptake and Biodistribution of Polymeric Nanoparticles. *Biomaterials* **2010**, *31*, 3657–3666.
33. Osaki, F.; Kanamori, T.; Sando, S.; Sera, T.; Aoyama, Y. A Quantum Dot Conjugated Sugar Ball and Its Cellular Uptake on the Size Effects of Endocytosis in the Subviral Region. *J. Am. Chem. Soc.* **2004**, *126*, 6520–6521.
34. Chithrani, B. D.; Ghazani, A. A.; Chan, W. C. W. Determining the Size and Shape Dependence of Gold Nanoparticle Uptake into Mammalian Cells. *Nano Lett.* **2006**, *6*, 662–668.
35. Lu, F.; Wu, S. H.; Hung, Y.; Mou, C. Y. Size Effect on Cell Uptake in Well-Suspended, Uniform Mesoporous Silica Nanoparticles. *Small* **2009**, *5*, 1408–1413.
36. Larsen, E. K. U.; Nielsen, T.; Wittenborn, T.; Birkedal, H.; Vorup-Jensen, T.; Jakobsen, M. H.; Ostergaard, L.; Horsman, M. R.; Besenbacher, F.; Howard, K. A.; *et al*. Size-Dependent Accumulation of PEGylated Silane-Coated Magnetic Iron Oxide Nanoparticles in Murine Tumors. *ACS Nano* **2009**, *3*, 1947–1951.
37. Lee, H. Y.; Lee, S. H.; Xu, C. J.; Xie, J.; Lee, J. H.; Wu, B.; Koh, A. L.; Wang, X. Y.; Sinclair, R.; Wang, S. X.; *et al.* Synthesis and Characterization of PVP-Coated Large Core Iron Oxide Nanoparticles as an MRI Contrast Agent. *Nanotechnology* **2008**, *19*, 165101.
38. Lu, X. Y.; Niu, M.; Qiao, R. R.; Gao, M. Y. Superdispersible PVP-Coated Fe_3O_4 Nanocrystals Prepared by a "One-Pot" Reaction. *J. Phys. Chem. B* **2008**, *112*, 14390–14394.
39. Wang, Y.; Ng, Y. W.; Chen, Y.; Shuter, B.; Yi, J.; Ding, J.; Wang, S. C.; Feng, S. S. Formulation of Superparamagnetic Iron Oxides by Nanoparticles of Biodegradable Polymers for Magnetic Resonance Imaging. *Adv. Funct. Mater.* **2008**, *18*, 308–318.
40. Sun, C. R.; Du, K.; Fang, C.; Bhattarai, N.; Veiseh, O.; Kievit, F.; Stephen, Z.; Lee, D. H.; Ellenbogen, R. G.; Ratner, B.; *et al*. PEG-Mediated Synthesis of Highly Dispersive Multifunctional Superparamagnetic Nanoparticles: Their Physicochemical Properties and Function *in Vivo*. *ACS Nano* **2010**, *4*, 2402–2410.
41. D'Souza, A. J. M.; Schowen, R. L.; Topp, E. M. Polyvinylpyrrolidone-Drug Conjugate: Synthesis and Release Mechanism. *J. Controlled Release* **2004**, *94*, 91–100.
42. Roca, A. G.; Veintemillas-Verdaguer, S.; Port, M.; Robic, C.; Serna, C. J.; Morales, M. P. Effect of Nanoparticle and Aggregate Size on the Relaxometric Properties of MR Contrast Agents Based on High Quality Magnetite Nanoparticles. *J. Phys. Chem. B* **2009**, *113*, 7033–7039.
43. Na, H. B.; Song, I. C.; Hyeon, T. Inorganic Nanoparticles for MRI Contrast Agents. *Adv. Mater.* **2009**, *21*, 2133–2148.
44. Koenig, S. H.; Kellar, K. E. Theory of $1/T_1$ and $1/T_2$ NMRD Profiles of Solutions of Magnetic Nanoparticles. *Mag. Res. Med.* **1995**, *34*, 227–233.
45. Jun, Y. W.; Huh, Y. M.; Choi, J. S.; Lee, J. H.; Song, H. T.; Kim, S.; Yoon, S.; Kim, K. S.; Shin, J. S.; Suh, J. S. Nanoscale Size Effect of Magnetic Nanocrystals and Their Utilization for Cancer Diagnosis *via* Magnetic Resonance Imaging. *J. Am. Chem. Soc.* **2005**, *127*, 5732–5733.
46. Yu, D. B.; Sun, X. Q.; Zou, J. W.; Wang, Z. R.; Wang, F.; Tang, K. Oriented Assembly of Fe_3O_4 Nanoparticles into Monodisperse Hollow Single-Crystal Microspheres. *J. Phys. Chem. B* **2006**, *110*, 21667–21671.
47. Jun, Y. W.; Lee, J. H.; Cheon, J. Chemical Design of Nanoparticle Probes for High-Performance Magnetic Resonance Imaging. *Angew. Chem., Int. Ed.* **2008**, *47*, 5122–5135.
48. Barick, K. C.; Aslam, M.; Lin, Y. P.; Bahadur, D.; Prasad, P. V.; Dravid, V. P. Novel and Efficient MR Active Aqueous Colloidal Fe_3O_4 Nanoassemblies. *J. Mater. Chem.* **2009**, *19*, 7023–7029.
49. Yang, H. M.; Lee, H. J.; Jang, K. S.; Park, C. W.; Yang, H. W.; Do Heo, W.; Kim, J. D. Poly(amino acid)-Coated Iron Oxide Nanoparticles as Ultrasmall Magnetic Resonance Probes. *J. Mater. Chem.* **2009**, *19*, 4566–4574.
50. Conner, S. D.; Schmid, S. L. Regulated Portals of Entry into the Cell. *Nature* **2003**, *422*, 37–44.
51. Jackson, H.; Muhammad, O.; Daneshvar, H.; Nelms, J.; Popescu, A.; Vogelbaum, M. A.; Bruchez, M.; Toms, S. A. Quantum Dots Are Phagocytized by Macrophages and Co-localize with Experimental Glioma. *J. Neuro-Oncol.* **2008**, *87*, 243.
52. Chen, F.; Ward, J.; Robinson, P. J. MR Imaging of the Liver and Spleen: A Comparison of the Effects on Signal Intensity of Two Superparamagnetic Iron Oxide Agents. *Magn. Reson. Imaging* **1999**, *17*, 549–556.
53. Ba-Ssalamah, A.; Uffmann, M.; Saini, S.; Bastati, N.; Herold, C.; Schima, W. Clinical Value of MRI Liver-Specific Contrast Agents: A Tailored Examination for a Confident Noninvasive Diagnosis of Focal Liver Lesions. *Eur. Radiol.* **2009**, *19*, 342–357.